Grafting amine-functionalized ligand layer on catalyst for electrochemical CO_2 capture and utilization

Zhikun Liu, Tao Yan, Han Shi, Hui Pan, Peng Kang [*]

School of Chemical Engineering and Technology, Tianjin University, Tianjin 300354, China

ARTICLE INFO

ABSTRACT

Direct electrochemical CO_2 capture and utilization from flue gas offers appealing route to closing the carbon cycle and avoiding the cost for CO_2 purification. Yet, the low CO_2 concentration in flue gas and competing oxygen reduction reaction (ORR) pose severe challenges for this process. Herein, we report 4-aminobutylphosphonic acid ligand layer capped Ag nanoparticles (NH_2BPA-Ag) for high-efficiency conversion of simulated flue gas (SFG). The amino group in NH_2BPA is available for CO_2 capture and activation, while phosphonic acid groups inhibit ORR by desorbing *OOH intermediate. NH_2BPA-Ag achieves 82% CO Faradaic efficiency (FE_{CO}) in H-cell for SFG reduction and enhances FE_{CO} 2.6 times over pristine Ag nanoparticles. In a membrane electrode assembly electrolyzer, NH_2BPA-Ag shows 79.6% FE_{CO} and 38.1% full-cell energy efficiency at 48 mA cm^{-2} for SFG conversion. This study highlights the strategy of tailoring catalytic microenvironments at molecular level for realizing a highly selective performance.

1. Introduction

Electrochemical carbon capture and utilization (CCU) using renewable electricity is a promising strategy for converting CO_2 to fuel and chemicals, which relieves the greenhouse effect and displaces fossil energy by sustainable carbon cycle [1–3]. Among the previous efforts for developing CO_2 reduction reaction (CO_2RR), electrocatalysts typically require high purity CO_2 feedstock to achieve efficient performance [4,5]. In fact, conventional CO_2 capture consists of multiple processes with high energy cost [6]. To execute CO_2RR at industrial scale, the CO_2 feedstock should come from abundant sources such as flue gas or air [7], which simplifies the process of CCU without the extensive energy for CO_2 purification [8]. However, the CO_2 concentration in flue gas is typically lower than 15%, accompanied by certain amount of oxygen and other minor impurities [9]. Consequently, flue gas electroreduction suffers from limited CO_2 mass transfer and the competition of oxygen reduction reaction (ORR) [10], owing to the favored thermodynamics of ORR [11]. Therefore, it is desirable to develop efficient electrocatalysts with capabilities of capturing CO_2 and inhibiting ORR for flue gas reduction.

In recent years, the strategy of modifying nanoparticles (NPs) with surface ligands has been investigated for creating controlled local environment at molecular level [12,13]. Certain ligands show strong electron interaction with the surface of NPs [14,15], and influence the mass transport of relevant reactants [16]. Furthermore, the interface between NP and ligand provides a favorable microenvironment for CO_2RR intermediates that greatly enhance catalytic activity [17]. However, it is challenging to simultaneously modulate the binding strength for different reactive species on the surface of catalyst [18]. Based on the nature of Lewis acid-base, amino groups are conducive to the adsorption of CO_2 and the formation of intermediates [19,20]. On the other hand, according to previous literatures in fuel cell, phosphonic acid doped proton exchange membranes could inhibit the kinetics of ORR, because phosphonic acids block active sites on catalysts for ORR [21,22], which provide inspiration to suppress ORR by grafting phosphonic acid groups on catalyst. Therefore, amino and phosphonic acid groups are critical to create appropriate catalytic environment for flue gas reduction.

Inspired by the above, we prepared functionalized Ag NPs by one-pot method for efficient production of CO from simulated flue gas (SFG, 15% CO_2, 4% O_2 and 81% N_2). Functional ligands, 4-aminobutylphosphonic acid (NH_2BPA) with both amino and phosphonic acid groups, were grafted on Ag NPs (NH_2BPA-Ag) to alter the surface environment. Experimental and theoretical calculations illustrated that amino groups significantly promoted the CO_2 capture on the NPs surface via chemical adsorption of CO_2, meanwhile the phosphonic acid groups reduced

* Correspondence to: School of Chemical Engineering and Technology, Tianjin University, 135 Yaguan Rd, Tianjin 300354, China.
E-mail address: kang.peng@tju.edu.cn (P. Kang).

available sites for ORR. Therefore, NH$_2$BPA-Ag could mimic the working mechanism of enzymes [23], which created a subtle microenvironment for molecular recognition and specific catalysis. As a result, NH$_2$BPA-Ag maintained a FE$_{CO}$ of 82.0% at −0.7 V vs. reversible hydrogen electrode (RHE) in H-cell under SFG, whereas Ag NPs without functional ligands lost most of its CO$_2$RR activity. In a membrane electrode assembly (MEA) electrolyzer for humid SFG conversion, the NH$_2$BPA-Ag catalyst exhibited 79.6% FE$_{CO}$ and 38.1% full-cell energy efficiency (EE) with a current density of 48 mA cm^{-2} at 2.8 V cell voltage. Overall, the functionalized modification could enhance the electrocatalytic selectivity of metal NPs in low CO$_2$ concentration conditions.

2. Experimental section

2.1. Chemicals

Silver nitrate (AgNO$_3$), NH$_2$BPA, butylamine (BNH$_2$), ethylene glycol (EG), glycerol, sodium chloride (NaCl) and potassium bicarbonate (KHCO$_3$) were purchased from Aladdin (China). poly(vinylpyrrolidone) (PVP-K30, average molecular weight~40000) was ordered from Yuanye (China). 1-butylphosphonic acid (BPA) was obtained from Bidepharm (China). All chemicals were used without further purification. The chemical structures of functional ligands used in this study are displayed in Fig. S1. Aqueous electrolyte solutions were prepared with deionized water (resistivity~18.2 MΩ·cm).

2.2. Synthesis of ligand-capped Ag NPs

NH$_2$BPA-Ag was prepared by a facile hydrothermal method. Firstly, 16.4 mg NaCl and 1.34 g PVP-K30 were dissolved in 20 mL EG to form a transparent PVP solution. At the same time, 0.69 g AgNO$_3$ was dissolved in 10 mL EG to make an Ag solution, and 31.1 mg NH$_2$BPA was dissolved in 10 mL EG to make a functionalized-ligand solution. Then the Ag solution and NH$_2$BPA solution were added into the as-prepared PVP solution under stirring. Afterwards, 8 mL glycerol was added in the above mixture and stirred for 1 min to form a colloidal solution. Subsequently, the colloidal solution was sealed in a 100 mL Teflon-lined stainless autoclave and maintained in an oven at 160 °C for 2 h. Finally, the precipitates were collected by centrifugation, and washed with ethanol, following by vacuum drying at 40 °C overnight to obtain NH$_2$BPA-Ag.

For comparison, BNH$_2$-functionalized Ag NPs (BNH$_2$-Ag) and BPA-functionalized Ag NPs (BPA-Ag) were prepared by a similar procedure except using BNH$_2$ and BPA as functional ligands, respectively, instead of NH$_2$BPA. In addition, unfunctionalized Ag NPs (Ag) were synthesized via similar route without the addition of functional molecules. In order to obtain PVP-removed Ag, Ag was stirred in 3 M KOH for 3 h, then rinsed with water, and dried under vacuum.

2.3. Characterizations

The morphology of the catalysts was characterized by a Hitachi Regulus 8100 field emission scanning electron microscope (SEM). Transmission electron microscopy (TEM) images, bright field scanning TEM (BF-STEM) images and energy dispersive X-ray (EDX) elemental maps of catalysts were obtained using a JEOL JEM-2100 F microscope at a 200 kV accelerating voltage. The samples were prepared by dropping catalyst powders in ethanol dispersion onto micro grids coated with carbon-film and dried in air. The X-ray diffraction (XRD) patterns of the catalysts were obtained by Bruker D8-Focus diffractometer equipped with Cu Kα radiation source, and the scanning speed was 5° min^{-1}. Fourier-transform infrared spectroscopy (FT-IR) measurements were recorded using a ThermoFisher Nicolet iS 50 FT-IR system. X-ray photoelectron spectroscopy (XPS) was measured using a ThermoFisher Kalpha spectrometer equipped with Al Kα source. The XPS spectra analysis was performed by Avantage software, and the data were calibrated by C 1 *s* peak at 284.8 eV. CO$_2$ isotherms were obtained by a

Quantachrome Autosorb IQ adsorption instrument, and samples were degassed for 6 h at 120 °C in vacuum before analysis. Density function theory (DFT) calculations were conducted by Vienna Ab initio Simulation Package (VASP) using the projector augmented wave (PAW) method, and the details were provided in Supporting Information.

2.4. Electrochemical measurements

The electrochemical tests were conducted by CHI660E electrochemical workstation using standard three-electrode system. For electrocatalytic measurements in H-cell, two compartments were separated by a cation exchange membrane (Nafion 117, DuPont). The Pt plate and the Ag/AgCl (saturated-KCl, Eilian) were used as counter electrode and reference electrode, respectively. In order to prepare catalyst ink, 5 mg catalyst was dispersed into 0.5 mL mixed solution containing 50 μL Nafion solution (5 wt%, DuPont), 100 μL H$_2$O and 350 μL ethanol, then sonicated for 20 min. After that, 20 μL ink was coated on a 0.5 cm × 0.5 cm carbon paper (Hesen) to prepare a working electrode. The anolyte and catholyte were 0.5 M KHCO$_3$ aqueous solution, and 15 mL catholyte was saturated with CO$_2$ gas (Air Liquide, 99.999%) or O$_2$ gas (Air Liquide, 99.999%) or purged by simulated flue gas (SFG, 15% CO$_2$, 4% O$_2$, 81% N$_2$) with a gas flow rate of 100 mL min^{-1} for 30 min prior to each electrochemical testing.

Linear sweep voltammetry (LSV) was carried out at a scan rate of 10 mV s^{-1}. Specially, LSV in aprotic electrolyte (0.1 M tetrabutylammonium hexafluorophosphate in dry acetonitrile, TBAPF$_6$/MeCN) were recorded on glassy carbon electrode loaded with catalysts, and Ag|Ag$^+$ electrode (10 mM AgNO$_3$/MeCN, Ida) was used as reference electrode. Controlled potential electrolysis (CPE) was performed with 80% ohmic compensation. Applied potentials were referenced to RHE using E (vs. RHE) = E (vs. Ag/AgCl) + 0.197 + 0.0591 × pH. Gas products were evaluated by a gas chromatograph (SRI 8610 C) equipped with helium ionization detector and thermal conductivity detector, using He (Air Liquide, 99.999%) as the carrier gas. FE$_{CO}$ was computed from dividing the number of consumed charges for CO by the total passed charges. Electrochemical impedance spectra (EIS) were conducted in SFG-bubbled 0.5 M KHCO$_3$ electrolyte with an amplitude of 5 mV in a frequency range of 100 mHz ~ 100 kHz (at −0.7 V vs. RHE). Electrochemical active surface area (ECSA) was evaluated by double-layer capacitance (Cdl) currents at various scan rates from 20 mV·s^{-1} to 120 mV·s^{-1}, the potential range was 0.35 ~ 0.45 V vs. RHE. The value of Cdl was twice the slope of linear fit of current.

2.5. SFG reduction tests in zero-gap electrolyzer

For the preparation of ink, 20 mg NH$_2$BPA-Ag, 20 mg carbon black and 100 μL Sustainion ionomer solution (5 wt%, Dioxide Materials) were dispersed into a mixture of 0.95 mL isopropanol and 0.95 mL H$_2$O followed by ultrasonication for 30 min. Then, the ink was sprayed on a carbon paper (SGL Carbon) at 70 °C, with the catalyst loading about 1.0 mg cm^{-2}. The catalyst-loaded carbon paper was used as cathode and IrOx supported on Ti mesh as anode. A Sustainion X37–50 (Dioxide Materials) anion exchange membrane (AEM) was pretreated in a 1 M KOH solution for 24 h, washed with water several times, then the AEM was sandwiched between cathode and anode for the fabrication of membrane electrode assembly (MEA, 4 cm^2 active area). After that, the MEA was placed in a customized cell with serpentine-type channels. SFG (200 sccm) passed through a 70 °C humidifier in order to maintain a high relative humidity (100%) at the inlet of cathode, while a 1 M KHCO$_3$ anolyte was made to circulate (10 mL min^{-1}) using a pump (BT100M, EasyPump). The electrochemical experiments were performed using a ITECH power supply. The full-cell EE of SFG conversion was calculated by the following equation:

$$EE = \frac{FE_{CO}E_{cell}^0}{E_{cell}}$$

where E_{cell}^0 is standard cell voltage ($=E_{water\ oxidation}^0 - E_{CO_2/CO}^0 = 1.23 - (-0.11) = 1.34$ V), E_{cell} is the applied cell voltage.

3. Results and discussion

3.1. Synthesis and physicochemical characterizations of catalysts

NH$_2$BPA-Ag was synthesized by a facile hydrothermal reaction (Fig. 1). In the process, NH$_2$BPA molecules as functional ligands could chemically bond on the Ag surface via phosphonic acid groups [17]. In fact, amino phosphonates have been used as multidentate ligands for the fabrication of polyoxometalates, and were stable in aqueous solution [24]. The carbonyl oxygen atoms of PVP capping agent bonded with surface Ag atoms to prevent NPs from growing [25]. Moreover, PVP could knit a thin organic layer on Ag NPs, which confined NH$_2$BPA to catalysts surface via non-covalent interactions (e.g., hydrogen bonds, and polar interactions, Fig S1) between PVP and NH$_2$BPA [26]. Alternatively, butylamine (BNH$_2$) and 1-butylphosphonic acid (BPA) molecules were also modified on Ag NPs by similar methods (noted as BNH$_2$-Ag and BPA-Ag). In addition, unfunctionalized Ag NPs were prepared by similar method without adding functional molecules, with only PVP on surface (noted as Ag).

The morphology and structure of catalysts were investigated by electron microscopy. SEM and TEM images confirm the nanoparticle morphology (average diameter $\approx$ 34 nm) of NH$_2$BPA-Ag, and all catalysts show similar morphology and size distribution (Fig. 2a, b and S2). Furthermore, Fig. 2c-e show that NH$_2$BPA-Ag is coated with a uniform organic layer with an approximate thickness of 2 nm. Such structure is also observed in BNH$_2$-Ag, BPA-Ag and Ag (Fig. S3). The high-resolution TEM (HRTEM) image shows that the spacing of lattice planes in NH$_2$BPA-Ag is 0.23 nm (Fig. 2e), which corresponds to the characteristic (111) facet of Ag [27]. As further evidence, the distribution of elements is analyzed by bright field scanning TEM (Fig. 2f), and the elemental mapping demonstrates homogenous distribution of C, N, and P elements throughout the catalyst (Fig. 2g), indicating that NH$_2$BPA molecules are uniformly anchored on the Ag NP surface.

The chemical bonding of ligand-capped Ag NPs was investigated by FT-IR. As shown in Fig. 3a, samples containing amino groups (NH$_2$BPA-Ag and BNH$_2$-Ag) display -NH$_2$ bending and N-H stretching at 1650 and 3200–3500 cm^{-1} respectively [8,28], while no such peaks are found in BPA-Ag and Ag. The bands at around 1050 cm^{-1} for BPA-Ag and Ag are attributed to the C-N stretching vibration of PVP [8]. The FT-IR spectra of NH$_2$BPA-Ag and BPA-Ag show the appearance of asymmetric and symmetric vibration of P-O bond at 970 cm^{-1}, and the bridge vibration of P-O-P at 560 cm^{-1}, proving the existence of phosphonic acid groups [29]. In addition, the characteristic peaks of functional groups in NH$_2$BPA-Ag are in agreement with the FT-IR spectrum of NH$_2$BPA (Fig. S4). XRD patterns (Fig. 3b) display that ligand-capped Ag catalysts mainly consist of metallic Ag, whereas small diffraction peaks of silver oxide are observed [30,31], and they would be reduced to Ag^0 under cathodic potential (Fig. S5). Furthermore, XPS measurements were employed to analyze the electronic structures and chemical features of ligand-capped Ag catalysts. As evidenced by Ag 3d spectra (Fig. 3c), Ag shows distinct doublet peaks at 367.7 and 373.6 eV, assigned to 3$d_{5/2}$ and 3$d_{3/2}$ of metallic Ag [31]. Notably, the Ag 3$d_{5/2}$ peak of BPA-Ag displays positive shift (368.4 eV), which is in accordance with reported alkylphosphonic acid modified Ag [17]. As for BNH$_2$-Ag, the binding energies of Ag 3d peaks are slightly lower than those in Ag, suggesting that BNH$_2$-Ag can donate electrons to Ag NPs [32]. These phenomena were considered as interfacial electronic effect [33], which would be discussed later. Notably, the Ag 3d peaks of NH$_2$BPA-Ag show a positive shift similar to that of BPA-Ag, which indicates that Ag surface strongly interacts with phosphonic acid groups, leaving amino groups available for CO$_2$ capture.

To further confirm the functionalization on the Ag NP surface, we performed N, P and O 1s XPS analysis of the catalyst. In the XPS N 1s spectrum of NH$_2$BPA-Ag (Fig. 3d), the nitrogen configurations are in the form of N-H (400.8 eV) and N-C (399.5 eV) bonds [8,34], and the higher proportion of N-C is due to the cumulative contribution of both NH$_2$BPA and PVP. The N 1s spectrum of BNH$_2$-Ag also reveals an obvious N-H signal of amino groups (Fig. S6), whereas BPA-Ag and Ag only show the C-N signals of PVP. In P 2p spectrum (Fig. 3e and S7), phosphonic acid modified catalysts (NH$_2$BPA-Ag and BPA-Ag) display obvious peaks of P at 132 eV. The O 1s spectrum (Fig. 3f) shows P=O signal at 533.1 eV belong to physisorbed state of phosphonic acid groups. Moreover, a peak located at 530.5 eV is due to the emergence of P-O-Ag bond in NH$_2$BPA-Ag, which suggests that the phosphonic acid groups can covalently bind with the Ag NP surface via oxygen atoms [35]. Therefore, NH$_2$BPA anchors on the surface of Ag NPs via phosphonic acid groups, while amino group faces the outside (Fig. 1). In addition, the C=O peak of PVP is observed at 531.7 eV for NH$_2$BPA-Ag [36], the same as other functionalized samples (Fig. S8), demonstrating the coexistence of functional molecules and PVP. The elemental contents on the surface of electrocatalysts were also obtained by XPS, as shown in Table S1, and the atomic percentages of N and P elements in NH$_2$BPA-Ag are 13.2% and 4.3%, respectively. In summary, the above results illustrate that the ligands can regulate the electronic structure of Ag surfaces by functional groups.
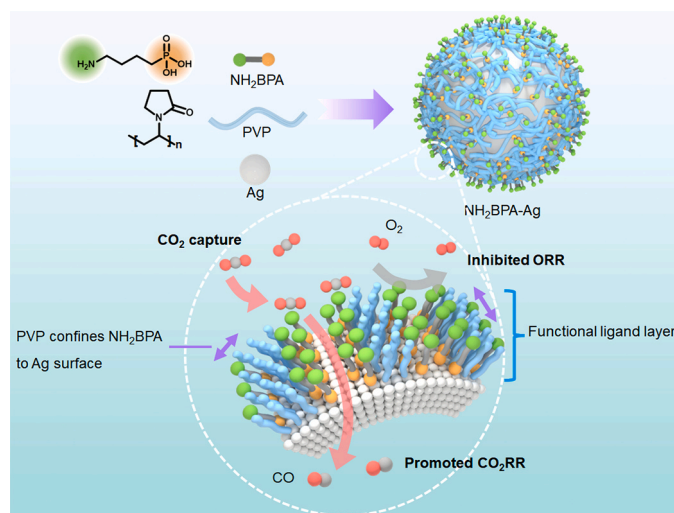

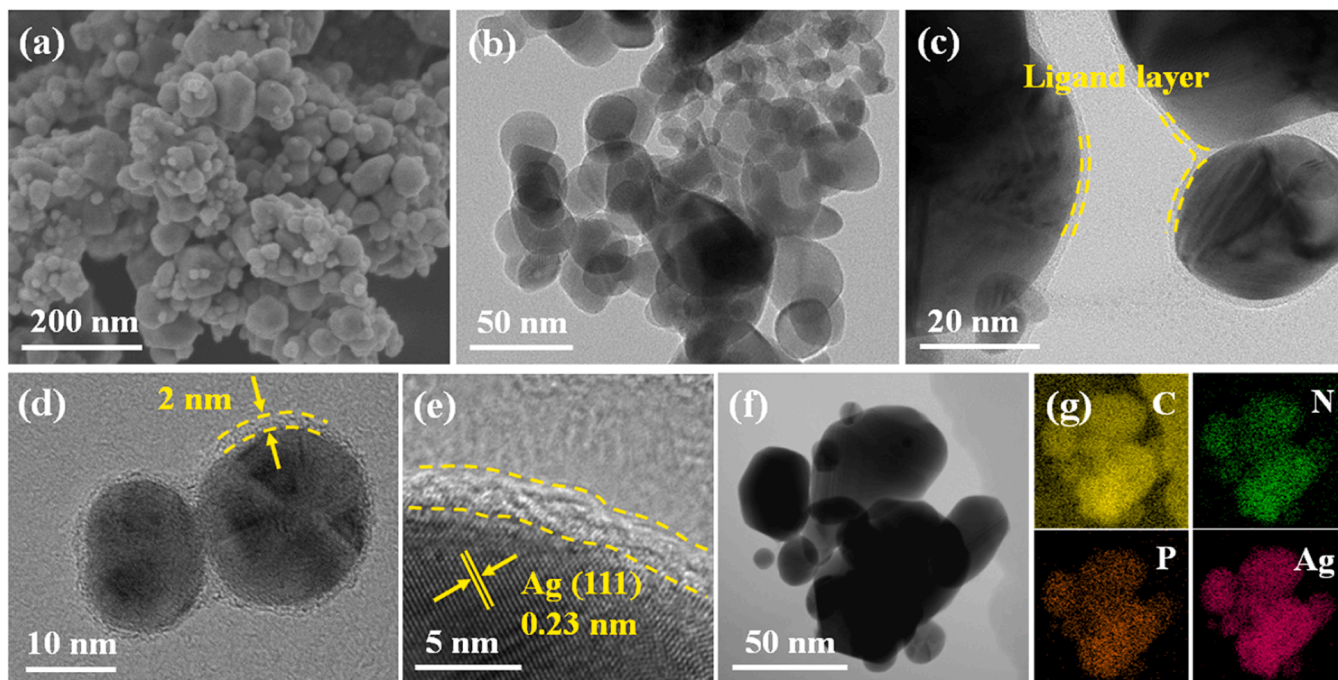**Fig. 1.** The fabrication of NH$_2$BPA-Ag with functional ligand layer.

Fig. 2. (a) SEM image, (b-d) TEM images and (e) HRTEM image of NH$_2$BPA-Ag. (f) Bright field STEM image and (g) elemental mappings of NH$_2$BPA-Ag.
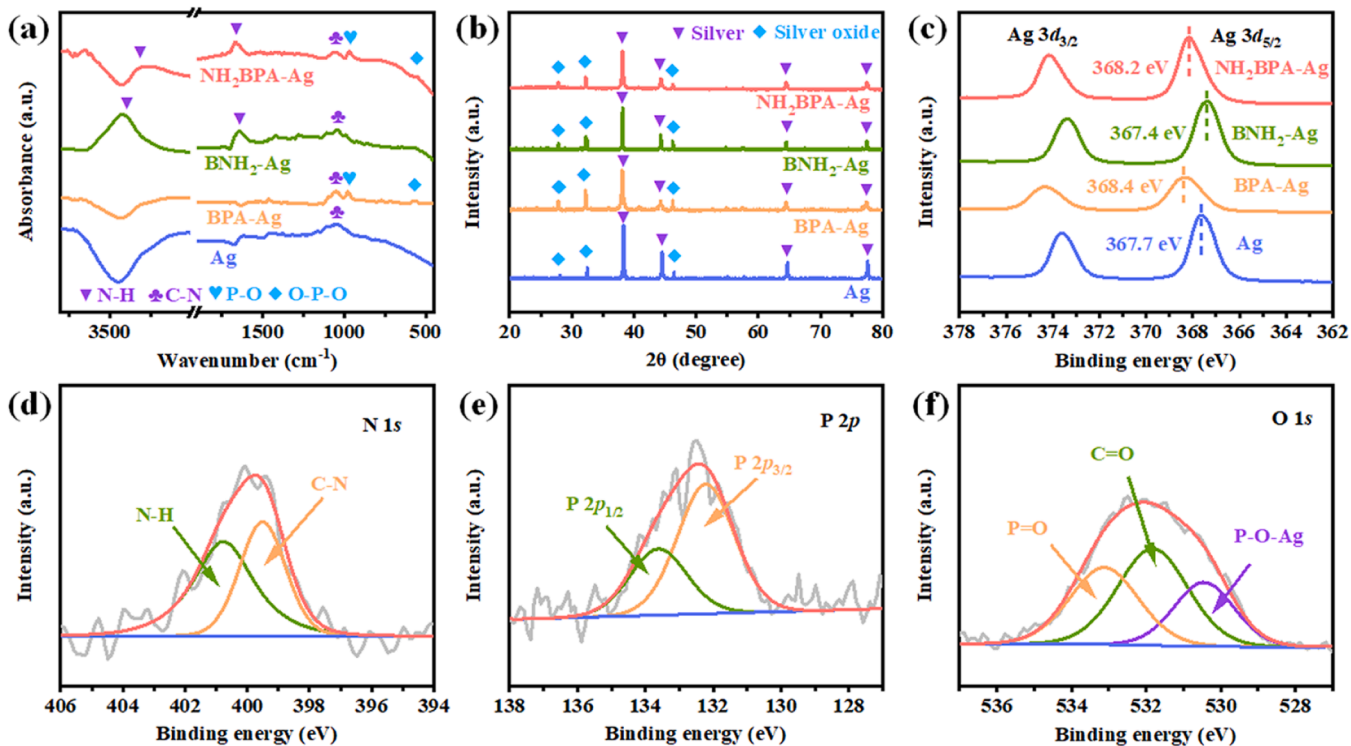

Fig. 3. (a) FT-IR spectra, (b) XRD patterns and (c) Ag 3d XPS spectra of catalysts. (d) N 1s, (e) P 2p and (f) O 1s XPS spectra of NH$_2$BPA-Ag.

3.2. Electrocatalytic activity evaluation of catalysts

Electrochemical measurements were first carried out in CO$_2$-saturated 0.5 M KHCO$_3$. LSVs were shown in Fig. S9, NH$_2$BPA-Ag exhibited more positive onset potential and increased current densities compared with other samples, suggesting the optimal activity. Controlled potential electrolysis (CPE) was performed on ligand-capped catalysts using pure CO$_2$, and the gaseous products were CO and H$_2$. NH$_2$BPA-Ag achieved maximum FE$_{CO}$ of 95.7% at −0.8 V vs. RHE (Fig. S10a), meanwhile, BNH$_2$-Ag, BPA-Ag and Ag showed FE$_{CO}$ of 86.6%, 84.2% and 80.1% at the same potential. Furthermore, NH$_2$BPA-Ag exhibited a CO partial current density (j$_{CO}$) of 33 mA cm^{-2} at −1.0 V vs. RHE (Fig. S10b), which was approximately 3 times higher than that of Ag. Comparing with reported literatures, NH$_2$BPA-Ag is among the state-of-the-art of Ag electrocatalysts and other metal-based materials for converting CO$_2$ to CO in H-cell configurations (Fig. S11) [14,37–40].

The electrochemical performance of catalysts was further investigated using SFG feedstock. The pH value of SFG-purged 0.5 M KHCO₃ electrolyte is 8.3, higher than that of CO_2-saturated (pH~7.2), due to the low CO_2 partial pressure in electrolyte. Fig. 4a and b show the FE_{CO} and total current density (j_{total}) for catalysts, NH₂BPA-Ag still exhibited higher CO selectivity compared to other catalysts, reaching the maximum FE_{CO} of 82.0% at −0.7 V vs. RHE, and the maximum j_{CO} of 10.6 mA·cm⁻² at −0.9 V vs. RHE. By contrast, BNH₂-Ag and BPA-Ag showed low FE_{CO} (53.1% and 43.4%, respectively) and j_{CO}. As for unfunctionalized Ag, it displayed inferior SFG reduction activity (31.8% FE_{CO}). Cyclic voltammograms were used to evaluate ECSA of electrocatalysts (Fig. S12). Upon NH₂BPA modification, a larger double-layer capacitance (9.7 mF·cm⁻²) was achieved for NH₂BPA-Ag (Fig. S13), higher than that of Ag (4.0 mF·cm⁻²), indicating increased ECSA [41]. Additionally, the Nyquist plot of NH₂BPA-Ag exhibited smaller resistance (Fig. S14), suggesting rapid charge transfer [42]. HRTEM was employed to survey on the surface of NH₂BPA-Ag after SFG electrolysis (Fig. S15), and the ligand layer remained on Ag surfaces. In addition, the N 1 *s* and P 2*p* spectra of NH₂BPA-Ag after CPE revealed that NH₂BPA still existed on the surface of NPs (Fig. S16). It was worth mentioning that PVP was innocent in CO_2 capture and electrocatalysis, when the PVP layer was eliminated from Ag surface, evidenced by HRTEM and XPS (Fig. S17a and b), comparable CO_2 adsorption capacity, FE_{CO} and j_{total} to that of Ag were recorded (Fig. S17c and d), suggesting that PVP could not significantly influence the activity for SFG conversion. Still, the ultrathin PVP layer provided microenvironment for confining functional ligands to catalysts surface via non-covalent interactions (Fig. S1) [26].

In order to investigate the specific function of the ligand layer, catalysts were evaluated under different atmospheres (Fig. 4c and S18): pure CO_2 gas, dilute CO_2 gas (DCG, 15% CO_2 + 85% N₂) and SFG. The NH₂BPA-Ag operating under DCG exhibited FE_{CO} of 89% and j_{total} of 10.5 mA·cm⁻², outperforming Ag with a FE_{CO} of 51.0% in the same condition. The j_{total} on amino-functionalized Ag NPs under CO_2 and DCG

were essentially the same (Fig. S18), indicating the promotion of CO_2 mass transfer. Under SFG condition, significant loss of FEs were noticed for both Ag and BNH₂-Ag due to parasitic ORR [43]. For phosphonic acid functionalized Ag NPs (NH₂BPA-Ag and BPA-Ag), FEs showed smaller missing loss, confirming the dominant role of the phosphonic acid groups in resisting O₂.

The catalytic intermediates were investigated using LSV in aprotic electrolyte (0.1 M TBAPF₆/MeCN). Without proton source for accomplishing proton-coupled electron transfer process in CO_2RR [44], LSV waves arose from the accumulation of $CO_2^{•-}$ intermediate (one electron reduced CO_2). Comparing LSV under Ar, NH₂BPA-Ag showed a current response at −2.5 V vs. Ag|Ag⁺ under CO_2 atmosphere (Fig. S19), corresponding to the formation of $CO_2^{•-}$. Under SFG atmosphere, catalysts with amino groups (NH₂BPA-Ag and BNH₂-Ag) exhibited much larger currents relative to others (Fig. 4d). It indicated that amino group could promote CO_2 adsorption and stabilize intermediates. The ORR activities of catalysts were investigated in O₂-saturated 0.5 M KHCO₃ solution via LSV experiments (Fig. 4e) [8]. An obvious ORR peak with a larger current density (3.1 mA cm⁻²) at the potential of 0.60 V vs. RHE was observed for Ag. Apparently, the ORR peaks of NH₂BPA-Ag and BPA-Ag showed much lower potentials (~ 0.46 V vs. RHE) and current densities (< 0.65 mA cm⁻²) than that of Ag, indicating that phosphonic acid groups increased the overpotential of ORR to slow the kinetics [21]. The higher capability of CO_2 adsorption on amino-functionalized Ag NPs were observed in Fig. 4f, further confirming the stronger interaction between amino groups and CO_2 [45].

To enhance the gas phase carbon capture, the electrocatalytic SFG reduction activity was investigated in zero-gap membrane electrode assembly (MEA) electrolyzer (Fig. 5a and S20) [31,47]. In this flow cell, the gas diffusion electrode (GDE) in cathode was pressed to an AEM, and humidified SFG (100% relative humidity) was directly passed to the cathode catalyst for gas-phase SFG reduction, while 1 M KHCO₃ was flowed in the anode (IrOₓ/Ti mesh). The catalytic activity of NH₂BPA-Ag was evaluated by CPEs (Fig. 5b and S21). The current density increased

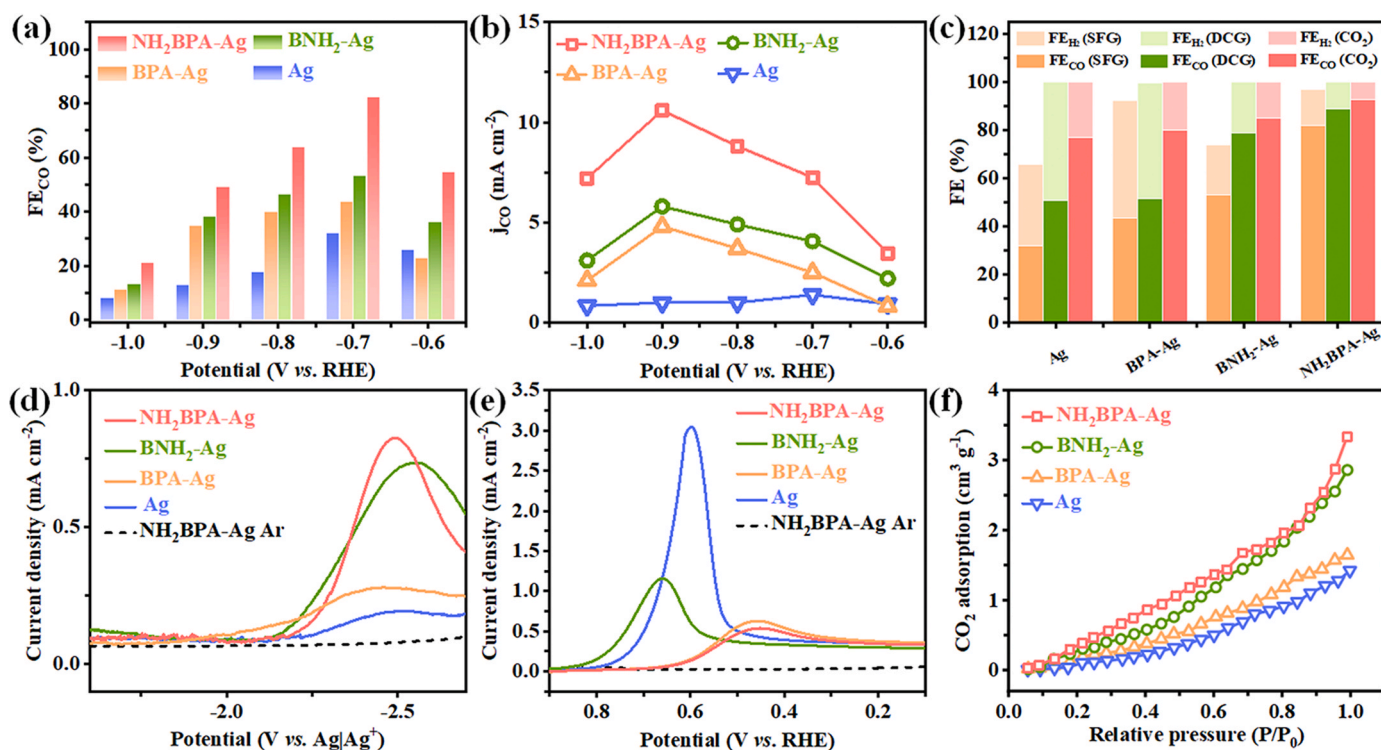**Fig. 4.** Potential-dependent (a) CO FEs and (b) CO partial current densities of catalysts in 0.5 M aqueous KHCO₃ under SFG condition (15% CO_2 + 4% O₂ + 81% N₂). (c) CO and H₂ FEs for catalysts operating at −0.7 V vs. RHE under CO_2, DCG (15% CO_2 + 85% N₂) or SFG. (d) LSVs of catalysts under SFG in 0.1 M TBAPF₆/MeCN. (e) LSVs of catalysts in O₂-saturated 0.5 M aqueous KHCO₃ electrolyte. (f) CO_2 adsorption isotherms of catalysts at 298 K.

with cell voltage, which exhibited high j_{total} of 48, 68, 95 mA cm^{-2} at cell voltage of 2.8, 2.9, 3.0 V, respectively, with maximum FE$_{CO}$ of 79.6% at a low voltage of 2.8 V. Owing to capturing properties of functional layer on catalyst as well as the zero-gap structure for fast CO$_2$ transfer, NH$_2$BPA-Ag MEA achieved higher current density and full-cell EE (38.1%) than state-of-the-art O$_2$-containing CO$_2$-to-CO electrolyzers (Fig. 5c and Table S2) [11,43,46], which could decrease the energy consumption and improve the process economics in electrochemical SFG conversion. Moreover, water vapor is an important component of flue gas, and the effect of humidity on electrochemical performance of MEA was further investigated. As shown in Fig. S22, compared with dry SFG, humidity had negligible impacts on FE$_{CO}$ and current density of NH$_2$BPA-Ag. This was owing to that the physisorption of water on catalysts is relatively weaker than chemisorption of CO$_2$ [43,48], thus the presence of amine maximized CO$_2$ availability even in humidity environment. The long-term electrolysis of NH$_2$BPA-Ag at the cell voltage of 2.8 V was also performed in MEA cell (Fig. 5d). The FE$_{CO}$ kept over 70% for 12 h, meanwhile, the current density nearly remained relatively stable during the entire period.

3.3. Mechanism study

To elucidate the origin of activity for ligand-functionalized Ag NPs, DFT calculations were performed to analyze the electronic structure and adsorption energy. Bader charge analysis showed that surface Ag atoms lacked electrons after phosphonic acid group chelating, whereas the amino group with lone-pair electrons negatively charged the surface Ag atoms (Fig. S23). These findings are consistent with the shifts in binding energy of Ag XPS (Fig. 3c), confirming the interfacial electronic effect caused by the modification of functional ligands [33]. The differential

charge diagram revealed that the amino group donated electrons to adsorbed CO$_2$ (Fig. 6a), enabling to activate CO$_2$ and enhance the activity of CO$_2$RR [45].

Electrochemical ORR could proceed via 4 e$^-$ pathway toward H$_2$O or 2 e$^-$ pathway toward H$_2$O$_2$, and both 4 e$^-$ and 2 e$^-$ pathways shared a common intermediate *OOH [49]. The adsorption energy of *OOH radical (ΔE *OOH) has been widely used to evaluate the activity of ORR [50,51]. When the substrate was changed from Ag to NH$_2$BPA-Ag, ΔE *OOH was changed from −1.42 to 1.35 eV (Fig. 6b), suggesting that the phosphonic acid group on Ag surface prevented the adsorption of *OOH and turned off ORR. Electron-rich surface atoms are more possibly to be ORR active sites [52]. As shown in Fig. 6c, Bader charge analysis revealed that Ag atoms (attached with *OOH) adjacent to phosphonic acid group had more electron depletion (−0.198 and −0.191 e$^-$), indicating less favorable chemical environment for ORR. This result further confirmed that phosphonic acid group had a significant effect on the neighboring Ag atom's electronic structure, which blocked ORR sites and benefit for improving the O$_2$ tolerance of catalysts.

As shown in Fig. S24, the positive shift of Ag 3d peaks continued to exist in post-CPE NH$_2$BPA-Ag, suggesting that the NH$_2$BPA ligands could steadily affect the surface electronic structure of Ag. Furthermore, the O 1 s spectrum of used NH$_2$BPA-Ag in Fig. 6d showed the increased content of phosphonate oxygens, indicating that partial P-O-Ag bonds transitioned to physisorbed state (-P=O/-P-O$^-$) under reduction potentials (Fig. 6e), and a new peak at the binding energy of 535.4 eV was attributed to the absorbed H$_2$O [17,29]. Based on above experimental and theoretical calculation, the enhanced SFG electrolysis performance of NH$_2$BPA-Ag can be explained by a possible mechanism shown in Fig. 6e. Benefiting from favorable adsorption and activation capability

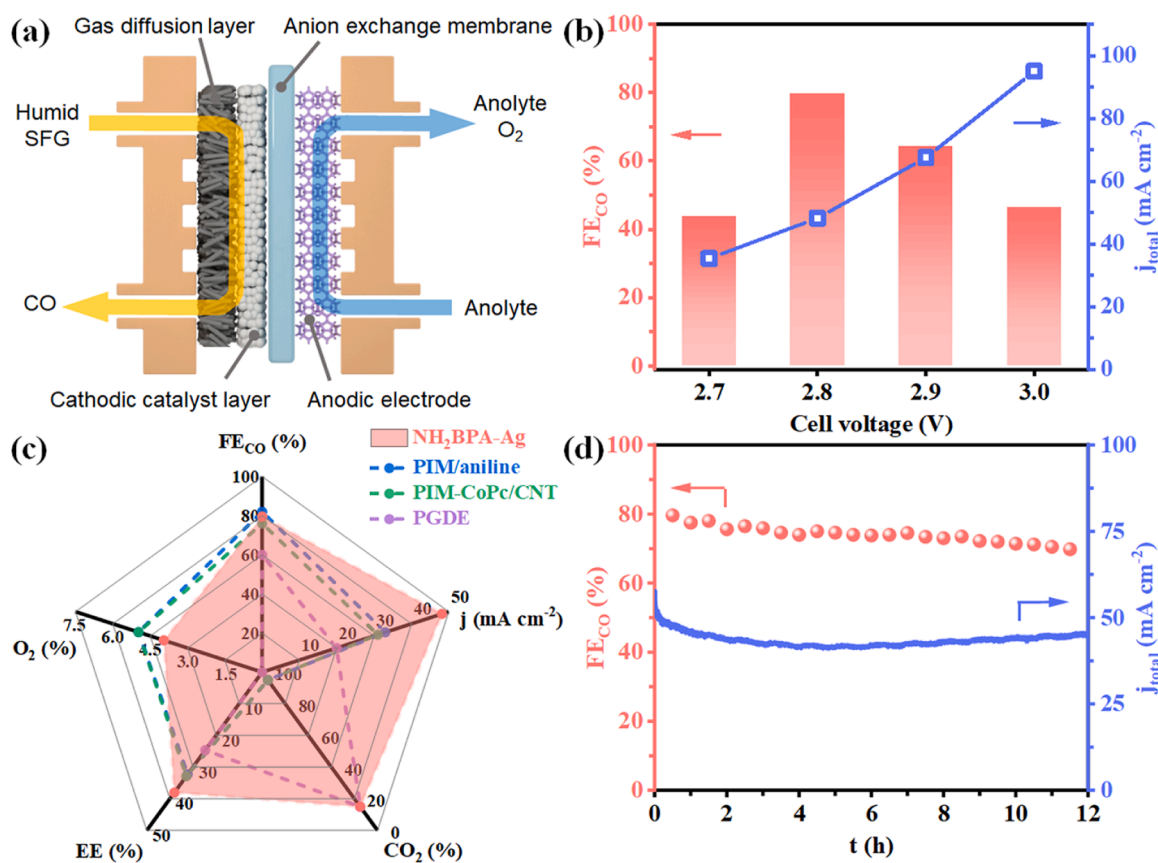**Fig. 5.** (a) Schematic illustration of a zero-gap MEA cell using AEM. (b) CO FEs and current densities vs. applied cell voltage on NH$_2$BPA-Ag for humid SFG electrolysis in MEA cell. (c) Spider chart of performance comparison between NH$_2$BPA-Ag and previously published data for flue gas electrolysis [11,43,46]. (d) Stability test of humid SFG electrolysis for NH$_2$BPA-Ag in MEA cell at 2.8 V.
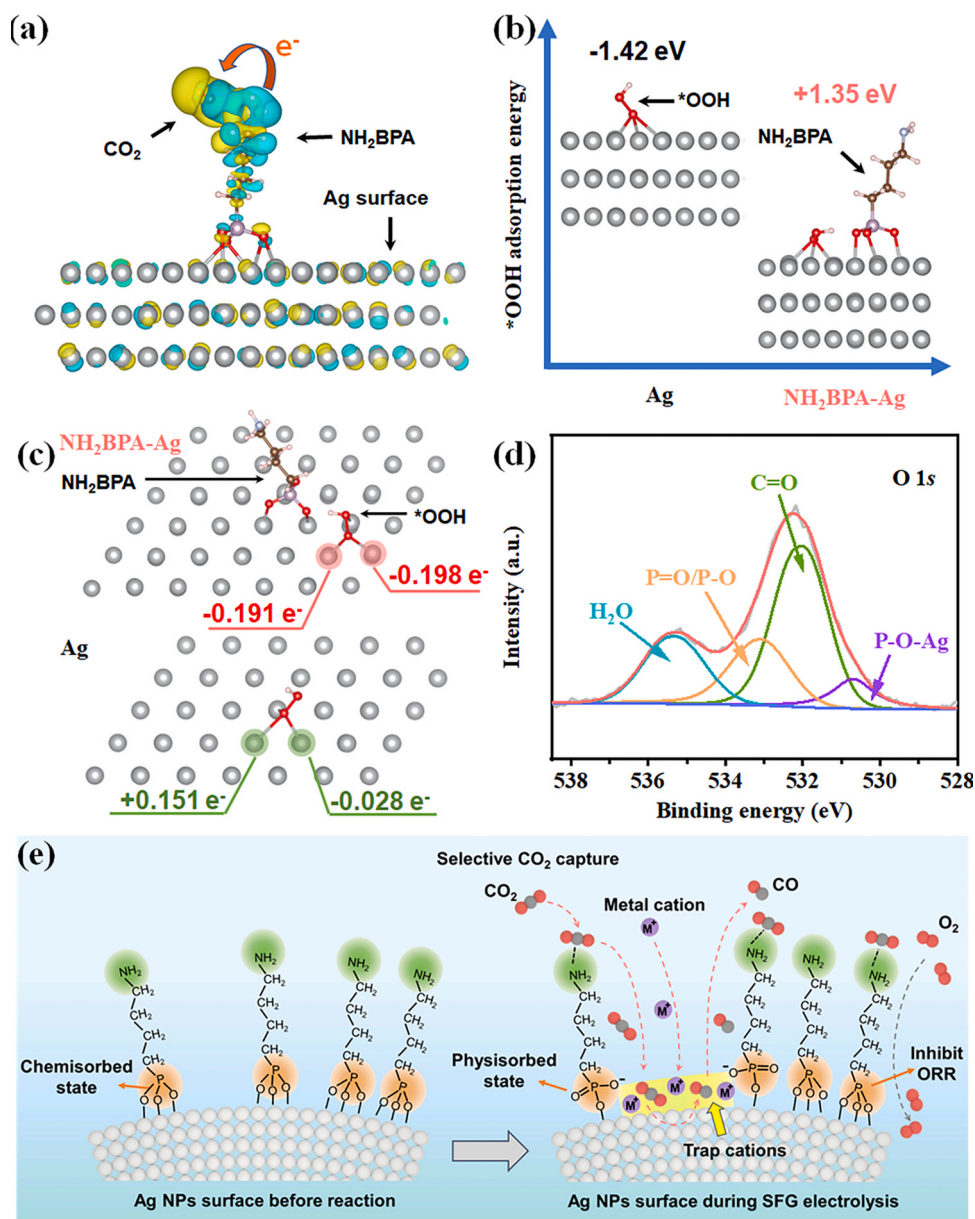
Fig. 6. (a) The differential charge density diagram of CO_2 adsorption on NH_2BPA-Ag. Yellow and cyan indicate accumulation and depletion of electrons, respectively. (b) Geometric structures and adsorption energies of *OOH intermediate on NH_2BPA-Ag and Ag. (c) Bader charge analysis of NH_2BPA-Ag and Ag with adsorbed *OOH. (d) O 1 s XPS for NH_2BPA-Ag after SFG electrolysis. (e) Schematic illustrating the proposed mechanism for SFG electrolysis over NH_2BPA-Ag.

for CO_2 of amino group, $CO_2^{\bullet-}$ was enriched on the surface of NH_2BPA-Ag. Meanwhile, phosphonic acid groups inhibited ORR by dissociating *OOH intermediate. Besides, the physisorbed phosphonic acid groups (-P-O⁻) with negative charges were able to trap abundant cations through electrostatic interactions nearing NP surface, enhancing the local electric field of double layer and promoting catalytic turnover [35,53], which was in agreement with the increased current density of catalysts modified by phosphonic acid group (Fig. S10b).

The length of carbon chain in ligand also affected the performance of electrocatalysis [14]. Although long carbon chains could enhance hydrophobicity of catalyst and reduced *H coverage, inhibiting hydrogen evolution [54], the increased distance between CO_2 trapping site and catalysts surface led to lower diffusion coefficient [55]. Short chain ligands were in favor of CO_2 transport but they were easier to dissociate from catalysts surface in aqueous electrolytes. Thus, the proper length of functional ligand was important to create a microenvironment for local CO_2 enrichment and reduction in aerobic environment.

4. Conclusions

In this study, the surface of Ag nanoparticles was capped by functional ligand layer, which was vital for efficient flue gas electro-reduction. After the modification, NH_2BPA-Ag demonstrated a maximum FE_{CO} of 82.0% at −0.70 V vs. RHE under SFG atmosphere. In contrast, the unfunctionalized Ag NPs only exhibited 31.8% of FE_{CO} in the same condition. Furthermore, we achieved SFG-to-CO conversion using a zero-gap MEA electrolyzer, which exhibited a j_{total} of 48 mA cm⁻² with a FE_{CO} of 79.6% at 2.8 V, and a full-cell EE up to 38.1%. The experimental results and DFT calculations suggested that the high activity of NH_2BPA-Ag was attributed to the synergistic effect of the head and tail groups in NH_2BPA ligand: the amino groups facilitated the CO_2 adsorption and activation, while the phosphonic acid groups bound the ligand to NPs and reduced the intrinsic activity of ORR. Collectively, this work reveals a prospective strategy that the specific microenvironments can be induced by the close cooperation of functional groups on ligands,

boosting the selectivity of catalysts under complicated conditions.

CRediT authorship contribution statement

Zhikun Liu: Conceptualization, Methodology, Investigation, Writing – original draft. **Tao Yan:** Validation. **Han Shi:** Validation. **Hui Pan:** Validation. **Peng Kang:** Conceptualization, Writing – review & editing.

Declaration of Competing Interest

The authors declare that they have no known competing financial interests or personal relationships that could have appeared to influence the work reported in this paper.

Data Availability

Data will be made available on request.

Acknowledgements

Appendix A. Supporting information

Supplementary data associated with this article can be found in the online version at doi:10.1016/j.apcatb.2023.123456.

References

[1] L. Li, X. Li, Y. Sun, Y. Xie, Rational design of electrocatalytic carbon dioxide reduction for a zero-carbon network, Chem. Soc. Rev. 51 (2022) 1234–1252.
[2] X. Zhang, Z. Zhang, H. Li, R. Gao, M. Xiao, J. Zhu, M. Feng, Z. Chen, Insight into heterogeneous electrocatalyst design understanding for the reduction of carbon dioxide, Adv. Energy Mater. 12 (2022), 2201461.
[3] S. Jeong, M.-H. Choi, G.S. Jagdale, Y. Zhong, N.P. Siepser, Y. Wang, X. Zhan, L. A. Baker, X. Ye, Unraveling the structural sensitivity of CO_2 electroreduction at facet-defined nanocrystals via correlative single-entity and macroelectrode measurements, J. Am. Chem. Soc. 144 (2022) 12673–12680.
[4] B.H. Ko, B. Hasa, H. Shin, E. Jeng, S. Overa, W. Chen, F. Jiao, The impact of nitrogen oxides on electrochemical carbon dioxide reduction, Nat. Commun. 11 (2020) 1–9.
[5] J.Y.T. Kim, P. Zhu, F.-Y. Chen, Z.-Y. Wu, D.A. Cullen, H. Wang, Recovering carbon losses in CO_2 electrolysis using a solid electrolyte reactor, Nat. Catal. 5 (2022) 288–299.
[6] S. Jin, M. Wu, R.G. Gordon, M.J. Aziz, D.G. Kwabi, pH swing cycle for CO_2 capture electrochemically driven through proton-coupled electron transfer, Energy Environ. Sci. 13 (2020) 3706–3722.
[7] M.C. Freyman, Z. Huang, D. Ravikumar, E.B. Duoss, Y. Li, S.E. Baker, S.H. Pang, J. A. Schaidle, Reactive CO_2 capture: a path forward for process integration in carbon management, Joule 7 (2023) 631–651.
[8] Y. Cheng, J. Hou, P. Kang, Integrated capture and electroreduction of flue gas CO_2 to formate using amine functionalized SnO_x nanoparticles, ACS Energy Lett. 6 (2021) 3352–3358.
[9] Y. Ma, X. Yi, S. Wang, T. Li, B. Tan, C. Chen, T. Majima, E.R. Waclawik, H. Zhu, J. Wang, Selective photocatalytic CO_2 reduction in aerobic environment by microporous pd-porphyrin-based polymers coated hollow TiO_2, Nat. Commun. 13 (2022) 1–10.
[10] Y. Xu, J.P. Edwards, J. Zhong, C.P. O'Brien, C.M. Gabardo, C. McCallum, J. Li, C.-T. Dinh, E.H. Sargent, D. Sinton, Oxygen-tolerant electroproduction of C_2 products from simulated flue gas, Energy Environ. Sci. 13 (2020) 554–561.
[11] X. Lu, Z. Jiang, X. Yuan, Y. Wu, R. Malpass-Evans, Y. Zhong, Y. Liang, N. B. McKeown, H. Wang, A bio-inspired O_2-tolerant catalytic CO_2 reduction electrode, Sci. Bull. 64 (2019) 1890–1895.
[12] G. Li, N. Marinkovic, B. Wang, M.R. Komarneni, D.E. Resasco, Manipulating the microenvironment of surfactant-encapsulated Pt nanoparticles to promote activity and selectivity, ACS Catal. 12 (2022) 13930–13940.
[13] Q. Zhu, C.J. Murphy, L.R. Baker, Opportunities for electrocatalytic CO_2 reduction enabled by surface ligands, J. Am. Chem. Soc. 144 (2022) 2829–2840.
[14] Y. Zhao, C. Wang, Y. Liu, D.R. MacFarlane, G.G. Wallace, Engineering surface amine modifiers of ultrasmall gold nanoparticles supported on reduced graphene oxide for improved electrochemical CO_2 reduction, Adv. Energy Mater. 8 (2018), 1801400.
[15] X. Cai, G. Li, W. Hu, Y. Zhu, Catalytic conversion of CO_2 over atomically precise gold-based cluster catalysts, ACS Catal. 12 (2022) 10638–10653.
[16] D. Wakerley, S. Lamaison, F. Ozanam, N. Menguy, D. Mercier, P. Marcus, M. Fontecave, V. Mougel, Bio-inspired hydrophobicity promotes CO_2 reduction on a Cu surface, Nat. Mater. 18 (2019) 1222–1227.
[17] S. Yu, D. Kim, Z. Qi, S. Louisia, Y. Li, G.A. Somorjai, P. Yang, Nanoparticle assembly induced ligand interactions for enhanced electrocatalytic CO_2 conversion, J. Am. Chem. Soc. 143 (2021) 19919–19927.
[18] R. Schlögl, Heterogeneous catalysis, Angew. Chem. Int. Ed. 54 (2015) 3465–3520.
[19] Z. Wang, Y. Zhou, C. Xia, W. Guo, B. You, B.Y. Xia, Efficient electroconversion of carbon dioxide to formate by a reconstructed amino-functionalized indium–organic framework electrocatalyst, Angew. Chem. Int. Ed. 60 (2021) 19107–19112.
[20] J. Su, J.-J. Zhang, J. Chen, Y. Song, L. Huang, M. Zhu, B.I. Yakobson, B.Z. Tang, R. Ye, Building a stable cationic molecule/electrode interface for highly efficient and durable CO_2 reduction at an industrially relevant current, Energy Environ. Sci. 14 (2021) 483–492.
[21] W. Li, D. Wang, T. Liu, L. Tao, Y. Zhang, Y.C. Huang, S. Du, C.L. Dong, Z. Kong, Yf Li, Doping-modulated strain enhancing the phosphate tolerance on ptfe alloys for high-temperature proton exchange membrane fuel cells, Adv. Funct. Mater. 32 (2022), 2109244.
[22] Z. Zhang, Z. Xia, J. Huang, F. Jing, X. Zhang, H. Li, S. Wang, G. Sun, Uneven phosphoric acid interfaces with enhanced electrochemical performance for high-temperature polymer electrolyte fuel cells, Sci. Adv. 9 (2023) eade1194.
[23] S.D. Fried, S.G. Boxer, Electric fields and enzyme catalysis, Annu. Rev. Biochem. 86 (2017) 387.
[24] Z.-X. Yang, X.-W. Liang, D. Lin, Q. Zheng, Y. Huo, Heteroatom-modulated assembly of hexalanthanoid-containing polyoxometalate-based coordination networks, Inorg. Chem. 62 (2023) 1466–1475.
[25] K. Wonner, S. Murke, S.R. Alfarano, P. Hosseini, M. Havenith, K. Tschulik, Operando electrochemical sers monitors nanoparticle reactions by capping agent fingerprints, Nano Res 15 (2022) 4517–4524.
[26] H. Zhang, W. Niu, S. Zhang, Extremely stretchable and self-healable electrical skin with mechanical adaptability, an ultrawide linear response range, and excellent temperature tolerance, ACS Appl. Mater. Interfaces 11 (2019) 24639–24647.
[27] K. Ye, T. Liu, Y. Song, Q. Wang, G. Wang, Tailoring the interactions of heterogeneous Ag_2S/Ag interface for efficient CO_2 electroreduction, Appl. Catal., B 296 (2021), 120342.
[28] J. Zhang, S. Deo, M.J. Janik, J.W. Medlin, Control of molecular bonding strength on metal catalysts with organic monolayers for CO_2 reduction, J. Am. Chem. Soc. 142 (2020) 5184–5193.
[29] X.Y. Zhang, W.J. Li, J. Chen, X.F. Wu, Y.W. Liu, F. Mao, H.Y. Yuan, M. Zhu, S. Dai, H.F. Wang, In operando identification of in situ formed metalloid zinc$^{\delta+}$ active sites for highly efficient electrocatalyzed carbon dioxide reduction, Angew. Chem. Int. Ed. 61 (2022), e202202298.
[30] J. Qin, Y. Dou, F. Wu, Y. Yao, H.R. Andersen, C. Hélix-Nielsen, S.Y. Lim, W. Zhang, In-situ formation of Ag_2O in metal-organic framework for light-driven upcycling of microplastics coupled with hydrogen production, Appl. Catal., B 319 (2022), 121940.
[31] W.H. Lee, C. Lim, E. Ban, S. Bae, J. Ko, H.-S. Lee, B.K. Min, K.-Y. Lee, J.S. Yu, H.-S. Oh, W@Ag dendrites as efficient and durable electrocatalyst for solar-to-CO conversion using scalable photovoltaic-electrochemical system, Appl. Catal., B 297 (2021), 120427.
[32] X. Gong, Y. Zhang, Y. Xu, G. Zhai, X. Liu, X. Bao, Z. Wang, Y. Liu, P. Wang, H. Cheng, Synergistic effect between CO_2 chemisorption using amino-modified carbon nitride and epoxide activation by high-energy electrons for plasmon-assisted synthesis of cyclic carbonates, ACS Appl. Mater. Interfaces (2022).
[33] G. Chen, C. Xu, X. Huang, J. Ye, L. Gu, G. Li, Z. Tang, B. Wu, H. Yang, Z. Zhao, Interfacial electronic effects control the reaction selectivity of platinum catalysts, Nat. Mater. 15 (2016) 564–569.
[34] X. Chen, J. Chen, N.M. Alghoraibi, D.A. Henckel, R. Zhang, U.O. Nwabara, K. E. Madsen, P.J. Kenis, S.C. Zimmerman, A.A. Gewirth, Electrochemical CO_2-to-ethylene conversion on polyamine-incorporated Cu electrodes, Nat. Catal. 4 (2021) 20–27.
[35] D. Kim, S. Yu, F. Zheng, I. Roh, Y. Li, S. Louisia, Z. Qi, G.A. Somorjai, H. Frei, L.-W. Wang, Selective CO_2 electrocatalysis at the pseudocapacitive nanoparticle/ordered-ligand interlayer, Nat. Energy 5 (2020) 1032–1042.
[36] Y. Zhang, H. Li, X. Zhang, H. Zhang, W. Zhang, H. Huang, H. Ou, Y. Zhang, Enhanced adsorption and photocatalytic Cr(VI) reduction and sterilization of defective MoS_2/PVP, J. Colloid Interface Sci. 630 (2023) 742–753.
[37] Y. Wang, L. Cao, N.J. Libretto, X. Li, C. Li, Y. Wan, C. He, J. Lee, J. Gregg, H. Zong, Ensemble effect in bimetallic electrocatalysts for CO_2 reduction, J. Am. Chem. Soc. 141 (2019) 16635–16642.
[38] Z. Zhang, G. Wen, D. Luo, B. Ren, Y. Zhu, R. Gao, H. Dou, G. Sun, M. Feng, Z. Bai, "Two ships in a bottle" design for Zn–Ag–O catalyst enabling selective and long-lasting CO_2 electroreduction, J. Am. Chem. Soc. 143 (2021) 6855–6864.
[39] W.H. Lee, Y.-J. Ko, Y. Choi, S.Y. Lee, C.H. Choi, Y.J. Hwang, B.K. Min, P. Strasser, H.-S. Oh, Highly selective and scalable CO_2 to CO-electrolysis using coral-nanostructured Ag catalysts in zero-gap configuration, Nano Energy 76 (2020), 105030.
[40] Q. Chen, K. Liu, Y. Zhou, X. Wang, K. Wu, H. Li, E. Pensa, J. Fu, M. Miyauchi, E. Cortés, Ordered Ag nanoneedle arrays with enhanced electrocatalytic CO_2 reduction via structure-induced inhibition of hydrogen evolution, Nano Lett. 22 (2022) 6276–6284.
[41] Z. Chen, X. Zhang, M. Jiao, K. Mou, X. Zhang, L. Liu, Engineering electronic structure of stannous sulfide by amino-functionalized carbon: Toward efficient electrocatalytic reduction of CO_2 to formate, Adv. Energy Mater. 10 (2020), 1903664.

[42] T. Dou, J. He, S. Diao, Y. Wang, X. Zhao, F. Zhang, X. Lei, Dynamic reconstructuring of CuS/SnO$_2$-S for promoting CO$_2$ electroreduction to formate, J. Energy Chem. 82 (2023) 497–506.

[43] T. Al-Attas, S.K. Nabil, A.S. Zeraati, H.S. Shiran, T. Alkayyali, M. Zargartalebi, T. Tran, N.N. Marei, M.A. Al Bari, H. Lin, Permselective MOF-based gas diffusion electrode for direct conversion of CO$_2$ from quasi flue gas, ACS Energy Lett. 8 (2022) 107–115.

[44] W. Zheng, D. Wang, W. Cui, X. Sang, X. Qin, Z. Zhao, Z. Li, B. Yang, M. Zhong, L. Lei, Accelerating industrial-level CO$_2$ electroreduction kinetics on isolated zinc centers via sulfur-boosted bicarbonate dissociation, Energy Environ. Sci. 16 (2023) 1007–1015.

[45] S. Cao, H. Liu, Z. Jia, M. Guo, W. Gao, Z. Ding, W. Yang, L. Chen, W. Wang, Controllable adsorption groups on amine-functionalized carbon nitride for enhanced photocatalytic CO$_2$ reduction, Chem. Eng. J. 455 (2022), 140746.

[46] P. Li, X. Lu, Z. Wu, Y. Wu, R. Malpass-Evans, N.B. McKeown, X. Sun, H. Wang, Acid–base interaction enhancing oxygen tolerance in electrocatalytic carbon dioxide reduction, Angew. Chem. Int. Ed. 59 (2020) 10918–10923.

[47] Z. Liu, T. Yan, H. Shi, H. Pan, Y. Cheng, P. Kang, Acidic electrocatalytic CO$_2$ reduction using space-confined nanoreactors, ACS Appl. Mater. Interfaces 14 (2022) 7900–7908.

[48] G. Rim, P. Priyadarshini, M. Song, Y. Wang, A. Bai, M.J. Realff, R.P. Lively, C. W. Jones, Support pore structure and composition strongly influence the direct air capture of CO$_2$ on supported amines, J. Am. Chem. Soc. 145 (2023) 7190–7204.

[49] J. Zhao, C. Fu, K. Ye, Z. Liang, F. Jiang, S. Shen, X. Zhao, L. Ma, Z. Shadike, X. Wang, Manipulating the oxygen reduction reaction pathway on Pt-coordinated motifs, Nat. Commun. 13 (2022) 685.

[50] Z. Sun, Y. Wang, L. Zhang, H. Wu, Y. Jin, Y. Li, Y. Shi, T. Zhu, H. Mao, J. Liu, Simultaneously realizing rapid electron transfer and mass transport in jellyfish-like Mott–Schottky nanoreactors for oxygen reduction reaction, Adv. Funct. Mater. 30 (2020), 1910482.

[51] J. Li, S. Wang, M.-F. Yue, S.-M. Xing, Y.-J. Zhang, J.-C. Dong, H. Zhang, Z. Chen, J.-F. Li, Graphene-isolated satellite nanostructure enhanced raman spectroscopy reveals the critical role of different intermediates on the oxygen reduction reaction, ACS Catal. 13 (2022) 849–855.

[52] Z. Li, H. Cheng, Y. Lu, T. Wang, Y. Li, W. Zhang, G. He, Z. Tian, Potent charge-trapping for boosted electrocatalytic oxygen reduction, Adv. Energy Mater. 13 (2023), 2203963.

[53] S. Ringe, E.L. Clark, J. Resasco, A. Walton, B. Seger, A.T. Bell, K. Chan, Understanding cation effects in electrochemical CO$_2$ reduction, Energy Environ. Sci. 12 (2019) 3001–3014.

[54] Y. Lin, T. Wang, L. Zhang, G. Zhang, L. Li, Q. Chang, Z. Pang, H. Gao, K. Huang, P. Zhang, Z.-J. Zhao, C. Pei, J. Gong, Tunable CO$_2$ electroreduction to ethanol and ethylene with controllable interfacial wettability, Nat. Commun. 14 (2023) 3575.

[55] W.A. Parada, D.V. Vasilyev, K.J. Mayrhofer, I. Katsounaros, CO$_2$ electroreduction on silver foams modified by ionic liquids with different cation side chain length, ACS Appl. Mater. Interfaces 14 (2022) 14193–14201.